PHOTONICS Research

Reconfigurable metasurface-based 1 × 2 waveguide switch

Amged Alquliah,[1,2] Mohamed Elkabbash,[3,4,5] Jinluo Cheng,[1,2,6] Gopal Verma,[1,2] Chaudry Sajed Saraj,[1,2] Wei Li,[1,2,7] and Chunlei Guo[3,8]

[1]GPL, Changchun Institute of Optics, Fine Mechanics and Physics, Chinese Academy of Sciences, Changchun 130033, China
[2]University of Chinese Academy of Sciences, Beijing 100049, China
[3]The Institute of Optics, University of Rochester, Rochester, New York 14627, USA
[4]Current address: The Research Laboratory of Electronics, Massachusetts Institute of Technology, Cambridge, Massachusetts 02139, USA
[5]e-mail: melkabba@mit.edu
[6]e-mail: jlcheng@ciomp.ac.cn
[7]e-mail: weili1@ciomp.ac.cn
[8]e-mail: guo@optics.rochester.edu

Received 22 April 2021; revised 13 August 2021; accepted 20 August 2021; posted 24 August 2021 (Doc. ID 428577); published 30 September 2021

Reconfigurable nanophotonic components are essential elements in realizing complex and highly integrated photonic circuits. Here we report a novel concept for devices with functionality to dynamically control guided light in the near-visible spectral range, which is illustrated by a reconfigurable and non-volatile (1 × 2) switch using an ultracompact active metasurface. The switch is made of two sets of nanorod arrays of TiO_2 and antimony trisulfide (Sb_2S_3), a low-loss phase-change material (PCM), patterned on a silicon nitride waveguide. The metasurface creates an effective multimode interferometer that forms an image of the input mode at the end of the stem waveguide and routes this image toward one of the output ports depending on the phase of PCM nanorods. Remarkably, our metasurface-based 1 × 2 switch enjoys an ultracompact coupling length of 5.5 μm and a record high bandwidth (22.6 THz) compared to other PCM-based switches. Furthermore, our device exhibits low losses in the near-visible region (~1 dB) and low cross talk (−11.24 dB) over a wide bandwidth (22.6 THz). Our proposed device paves the way toward realizing compact and efficient waveguide routers and switches for applications in quantum computing, neuromorphic photonic networking, and biomedical sensing and optogenetics.

https://doi.org/10.1364/PRJ.428577

1. INTRODUCTION

The advancement of nanofabrication, coupled with the attainment of a high level of complexity in photonic integrated circuits (PICs), triggered tremendous interest toward realizing miniaturized all-optical interconnects that are superior to electronic circuits in terms of bandwidth density, speed, and energy efficiency as well as mitigating the von Neumann data transmission bottleneck [1–3]. Particularly, the reconfigurable control of light propagating in PICs is crucially important for many emerging applications such as programmable PIC [4], neuro-inspired computing [5,6], quantum information processing [7,8], optical communication [9,10], microwave photonics [11], and sensor applications [12,13].

Reconfigurable photonic computing cores are conventionally implemented using waveguide meshes of Mach–Zehnder interferometers (MZIs) where the interference is controlled via two phase shifters that are independently tuned through volatile and weak modulation of the waveguide refractive index commonly using electro-optic or thermo-optic effects [4], leading to devices with a limited tunability, high energy consumption [several milliwatts (mW)], and large footprints [hundreds of micrometers (μm)] [14]. On the other hand, micro-ring resonators (MRRs) [15–20] and micro-electromechanical systems (MEMS) [21,22] offer high modulation depth and a relatively small footprint. Still, they suffer from a narrow operational bandwidth (less than 3 dB) [20], low tolerance to temperature variations and fabrication errors, as well as a large actuation voltage (>40 V) [23]. Notably, systems based on exciting surface plasmon resonances (SPRs) enjoy the highest switching rates and smallest footprints. However, they suffer from high insertion and propagation losses as they require coupling from/to a photonic waveguide [24,25], and plasmonic metals

are highly lossy [25], which hinder their widespread usage. The common volatility of these schemes necessitates an "always-on" power supply to retain the switching state, rendering them energy inefficient [14,26].

To circumvent these hurdles, phase-change materials (PCMs) emerged as candidates to demonstrate photonic reconfigurability owing to their unique tunable properties [27,28]. PCMs possess high contrasts in the electrical resistivity and refractive index between the resonant-bonded crystalline and covalent-bonded amorphous phase states over a wide spectral range. They are non-volatile, reversible, and they provide fast and low energy actuation (<10 aJ/nm^3 [29]) by ultrashort electrical or optical pulses (up to subnanosecond) [30] and stable switching ability of more than 10^{15} cycles [31]. In addition, the scalability of PCMs makes their nanofabrication relatively approachable and compatible with other substrates, as their amorphous state is used during deposition [23]. Several PCM-based integrated photonic devices were recently demonstrated, e.g., photonic memories [32,33], optical modulators [34,35], optical switches [14–20], and optical computing [36,37]. In these applications, a top-cladding layer of $Ge_2Sb_2Te_5$ (GST) and, recently, $Ge_2Sb_2Se_4Te_1$ (GSST) was deposited onto a waveguide. However, the high absorption losses in one of the phases of such materials fundamentally restrict their use in phase modulation schemes for large-area PICs [4] and deep-neural networks [5,6], where light would propagate through several PCM-based interconnects. Although losses can be alleviated in devices working at the telecom wavelengths, this comes with the cost of sacrificing the device footprint. In addition, such approach is impractical at the visible and near-visible wavelengths due to the large intrinsic losses. Finally, the use of large-area PCMs creates a considerable barrier to the actuation mechanism (see Appendix A for more details).

On the other hand, optical metasurfaces enable unprecedented flexibility in controlling the propagation of light through a spatially dependent and abrupt phase change at an interface that is imposed by ultrathin artificial arrays of engineered subwavelength nanoantennas [38]. Metasurfaces have realized a plethora of ultracompact, broadband, and efficient on-chip photonic devices, such as mode converters [39], polarization rotators [39], mode-pass polarizers [40], power splitters [41], asymmetric power transmitters [39], second-harmonic generators [42], remote near-field controllers [43], and guided waves to free space wave couplers [44–46]. However, these devices are passive and application specific because the optical properties of the constitutional meta-atoms are permanent once fabricated. To actively tune the optical properties of metasurfaces, several approaches have been introduced [47,48] with considerable interest in using PCMs [28,49] due to their advantages as discussed above. So far, such investigations on reconfigurable metasurfaces are focusing on controlling light propagating in free space, e.g., for bichromatic and multifocus Fresnel zone plates [50], beam steering [31], tunable color generators [51], dynamic spectrum controllers [52], switchable spectral filters [53], information processing [54], communication [55], imaging [56], hologram and augmented reality [57–59], vortex beam generators, and illusion and cloaking [60].

In this paper, we extend the concept of reconfigurable metasurfaces to PICs by reporting a novel dynamic near-visible nanophotonic (1×2) switch enabled by combining two nanorod arrays of TiO_2 and a novel ultralow-loss PCM (antimony trisulfide Sb_2S_3) superimposed on silicon nitride waveguide. Our designed device provides unprecedented functionality as it facilitates the non-volatile dynamic routing of light inside a multimode waveguide toward predefined outputs. The device shows a wide bandwidth of 22.6 THz, low loss (~1 dB), and low cross talk (<-11.29 dB) with a compact active length (5.5 μm). To the extent of our knowledge, our design enjoys a record footprint compared to PCM-based optical switches, which would overcome the challenges associated with large-area PCM actuation. Table 1 compares the design principles, the type of PCM designs, and performance of the reported (1×2) PCM-based switches and of our metasurface PCM-based switch. Appendix B discusses the need for visible/near-visible PICs.

2. MATERIALS AND METHODS

Figure 1(a) schematically illustrates the structure and functionality of our device, which is a Y-branch waveguide with a metasurface located on the surface of its stem. From bottom to top, the waveguide is formed by a silicon substrate, a 3 μm thick SiO_2 layer, and a ridge SiN waveguide. The metasurface consists of two sets of nanorods. Each set includes 28 equally spaced nanorods with a length L and a center-to-center distance between neighbor nanorods Λ. These two sets are aligned to form two adjacent rectangles separated by a gap g. The total footprint of the metasurface is L_x.

The materials are chosen to realize a device appropriate for near-visible integrated photonics. The SiN waveguide has the

Table 1. Comparison of Previously Reported PCM-Based (1×2) Switches with Our Metasurface-Based Switch

Design Principle	PCM Design	Bandwidth (THz)	Cross Talk (dB)	Operating Wavelength Range	Reference
Directional coupler	GST layer	3.74	−10	IR	[14]
Directional coupler	GSST layer	4.4	−32	IR	[61]
Contra-directional coupler	GST-Si grating	0.275	−30	IR	[62]
Micro-ring resonator	GST layer	0.125	−6	IR	[16]
Micro-ring resonator	GST layer	0.125	−33	IR	[17]
Micro-ring resonator	GST layer	0.125	−42	IR	[18]
Micro-ring resonator	GST layer	0.125	−5	IR	[15]
Micro-ring resonator	GST nanodisk	0.125	−5	IR	[20]
Micro-ring resonator	GST layer	0.125	−14.1	IR	[19]
Micro-ring resonator	Sb_2S_3 layer	0.125	NA	Visible	[63]
Y branch	**Sb_2S_3/TiO_2 metasurface**	**22.6**	**−11.24**	**Near visible**	**This work**

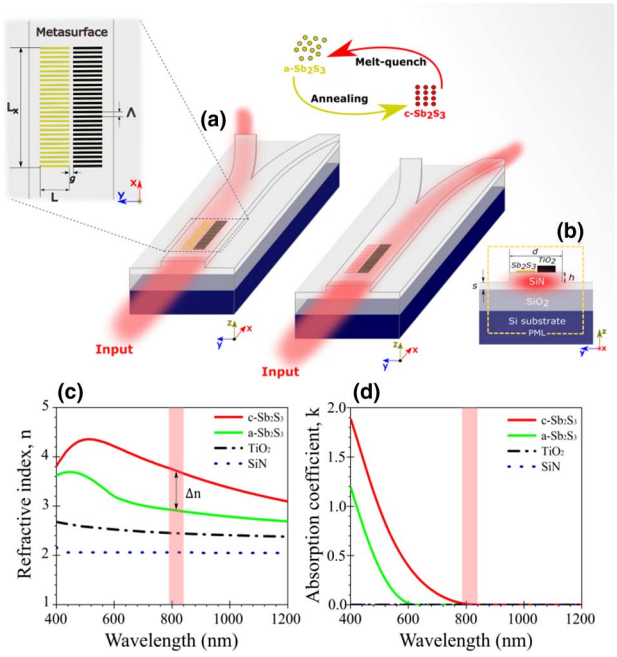

Fig. 1. Design of the proposed metasurface-based reconfigurable (1 × 2) integrated switch working around $\lambda = 800$ nm. (a) 3D illustrations of the device structure and its functionality when the Sb_2S_3 metasurface structure is in a crystalline or amorphous state. The top-left inset shows the top view of the device with dimensions of the metasurface consisting of a set of passive TiO_2 nanorods and another set of PCM (Sb_2S_3) nanorods. The top middle inset shows the conditions required for the Sb_2S_3 to undergo a reversible structural transition from amorphous to crystalline states. (b) Cross section of the device. (c) and (d) Wavelength dependence of the complex optical constants (n, k) of amorphous Sb_2S_3, crystalline Sb_2S_3, amorphous titanium dioxide, and silicon nitride. Highlighted parts in red indicate the spectral region of interest where Sb_2S_3 exhibits low loss and high switching contrast.

advantages of thermodynamic stability, wide spectral range of transparency ($\lambda = 0.25$–8 μm), higher fabrication flexibility, and lower propagation losses compared to silicon waveguides [64]. The materials of the two sets of nanorods are chosen as PCM antimony trisulfide (Sb_2S_3) for one set and amorphous titanium dioxide (a-TiO_2) for the other. Compared to the prototypical PCM (GST), the new class of PCM (Sb_2S_3) has a bandgap tunable from 2.0 eV (crystalline) to 1.7 eV (amorphous), and thus it works in the near-visible spectrum with a low absorption coefficient and a relatively higher contrast in the change of the real part of its refractive index Δn [65–67]. A-TiO_2 is chosen because it is lossless in the near-visible range and enjoys a high refractive index to provide strong guided light–nanorod interaction [68]. The top middle inset in Fig. 1(a) shows the reversible optical switching of the Sb_2S_3 from the crystalline to amorphous phases. The optical switching [65–67] can be done using a 630 nm laser source with a power of up to 90 mW. This laser source provides stable performance and cycling durability of Sb_2S_3 during the experiment [67]. The reversible switching between both structural states of Sb_2S_3 is realized by controlling the width and focus of the laser pulse [67]. The crystallization process requires pulses with long time duration (100 ms) [67] to reach the Sb_2S_3 glass transition temperature at 270°C [67]. In contrast, the re-amorphization process requires pulses with shorter time duration (400 ns) [67] to reach the Sb_2S_3 melting temperature at 527.85°C [67] and then quickly cool it at a rate >20°C/ns [53,67,69].

In our designed metasurface, the nanorod antennas cause a spatial linear phase shift of the optical mode in the waveguide in addition to the propagation phase along the propagation direction (x axis). The accumulative local phase shifts from the two nanorod sets result in a constructive interference that focuses the input fundamental mode in the stem multimode waveguide. Following that, the focused input mode partially converts the input fundamental mode to higher-order modes, creating an effective asymmetric multimode interferometer (MMI). Consequently, an image of the input mode is formed at the end of the stem multimode waveguide due to the self-imaging principle of the MMI [70]. The produced image is then routed in one of the predefined output ports depending on the phase of the PCM nanorods (specifically depending on the effective refractive index of the nanorod arrays). Therefore, when Sb_2S_3 is in the crystalline state, it has a significantly higher effective index, causing a larger phase delay at the side where the PCM nanorods are located. In contrast, when the Sb_2S_3 is in the amorphous state, the TiO_2 causes a larger phase delay at the other side of the waveguide, leading to the field constructively interfering at the opposite side.

The optical properties of the device were simulated using the finite-difference time-domain method (FDTD, Mode Solutions, Lumerical Ansys Inc.). The simulation domain was enclosed by eight standard perfectly matched layers as boundary conditions. To minimize the numerical dispersion and to enhance the interfaces' resolution, we chose the nonuniform auto mesh setting with a minimum size of conformal mesh cell of 2.5 nm. The fundamental TE mode was launched into the stem SiN waveguide using a broadband mode source and enabling multifrequency calculations. The frequency-domain time power monitors were used to record the profile of the normalized electric field intensity, transmission at output ports, reflection, and scattering. For calculating the effective indices as well as the dispersion in the SiN waveguide, the finite-difference eigenmodes solver (FDE, Mode Solutions, Lumerical Ansys Inc.) was used. To estimate the effective indices of metasurface nanorod arrays, the effective medium theory was considered by using Rytov's approximations.

To optimize the device performance, the ridge SiN multimode waveguide is chosen to have a rectangular shape with a height $h = 220$ nm, a thickness of under-etched layer $s = 200$ nm, and a sufficiently large width $d = 3.5$ μm to support the multimode interference and to reduce the cross talk between the output ports [70] [see Fig. 1(b)]. Note that the two output waveguides are narrower to match the spot size of the produced single self-images and optimize the device cross talk. The mode of the output waveguides can be coupled with other devices with arbitrary widths using techniques such as waveguide tapers [71–74] or integrated mode size converters [75–77]. Appendix C shows the dependence of effective refractive indices and dispersion of modes on the width of the SiN

waveguide. The two output ports have a width $d_{out} = 1.65$ μm and are attached to the end of the stem waveguide at a position where the self-image is formed. During the simulation, the complex optical constants of SiN, SiO_2, Si, and TiO_2 are obtained from the database of Palik [78], while the experimental values of Sb_2S_3 are taken from Refs. [67,79]. Figures 1(c) and 1(d) list the optical constants of a-TiO_2, SiN, and two phases of Sb_2S_3. To compromise between the absorption coefficient (k) and the refractive index contrast (Δn), the operating bandwidth is set around 800 nm as shown in the red bars in Figs. 1(c) and 1(d).

The performance metrics of a waveguide optical switch are the cross talk and the transmission, where the former is defined as the contrast transmission ratio between the two output ports [14]. Although it is not easy to define a qualitative quantity for the performance metric, an efficient optical switch should exhibit low cross talk and high transmission. The metasurface was engineered adopting the direct design approach [80]. To obtain the target performance, first, the width ($W_{Sb_2S_3}$) and height (h_s) of Sb_2S_3 nanorods were fixed at ($W_{Sb_2S_3} = 55$ nm, $h_s = 50$ nm) to support Mie resonant modes in the nanoantennas [39,42,81,82] and to meet the current state of manufacturing capacity [65,66]. The period (Λ) was set at 200 nm to avoid diffraction effects [83,84]. Following that, the dimensions of TiO_2-nanorods (width and height) were optimized to realize the desired optical routing response (see Appendix D for further details). The gap width (g) between the two nanorod sets was kept at 180 nm to bring about degrees of freedom to the metasurface fabrication. Finally, L_x, L, g, and Λ were parametrically swept in sequential order as shown in Figs. 2(a)–2(d). The final dimensions of the metasurface are as follows: the TiO_2 nanorods have a width of 72 nm and a thickness of 250 nm; $\Lambda = 200$ nm, $L = 1060$ nm, $g = 180$ nm, and $L_x = 5.5$ μm, indicating an ultracompact footprint (Fig. 2, inset). The suggested fabrication method and working setup of the proposed device are provided in Appendix E.

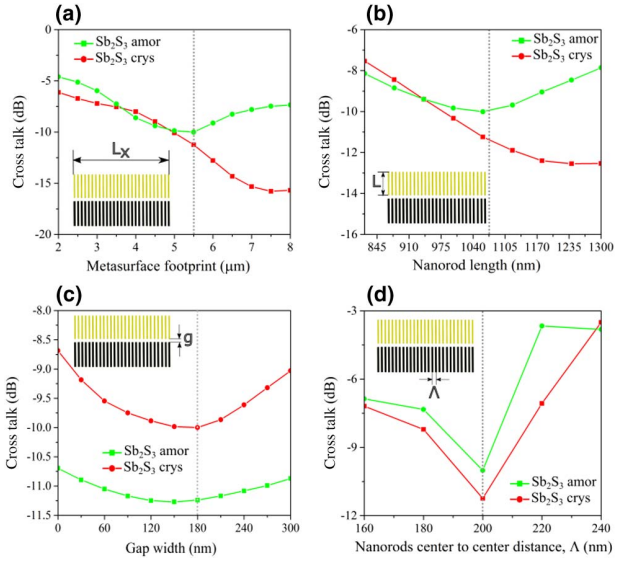

Fig. 2. Metasurface parametric sweep. (a)–(d) Device cross talk as a function of metasurface footprint (L_x), nanorod length (L), separated gap width (g), and the nanorods' center-to-center distance (Λ), respectively, for a-Sb_2S_3 and c-Sb_2S_3. The dotted gray lines show the dimensions used in our metasurface.

3. RESULTS AND DISCUSSION

Before presenting the functionality of the metasurface, it is instructive to characterize how the single metasurface nanoantenna confines the light inside the waveguide. Figures 3(a) and 3(b) show the calculated field distribution (E_z components) and the electric field intensity $|E|^2$ distribution in the nanorods and for both phases of Sb_2S_3. In our design, the dimensions of the TiO_2 nanorods are larger than those of the Sb_2S_3 nanorods in order to increase the magnitude of phase delay (i.e., effective refractive index) and compensate for its lower refractive index compared to a-Sb_2S_3. Therefore, for a-Sb_2S_3, the field is mostly confined in the TiO_2 nanorod. When the PCM changes its state to c-Sb_2S_3, the field becomes strongly confined in the Sb_2S_3 rods. Figure 3(c) shows the length dependence of the calculated effective refractive index for different nanorod antennas positioned on the SiN substrate at $\lambda = 800$ nm. The FDE method was implemented to obtain the effective refractive indices caused by metasurface nanoantennas. A significant n_{eff} difference is obtained between a-Sb_2S_3 and c-Sb_2S_3 antennas due to their high refractive index contrast. The n_{eff} of TiO_2 lies between the n_{eff} of a-Sb_2S_3 and c-Sb_2S_3, which in turn partly explains the switching functionality of our device. Appendix F discusses the method used for calculating the equivalent effective indices of the Sb_2S_3 and TiO_2 nanorod arrays. These results show that employing high-index dielectric/PCM nanoantennas on a waveguide offers a unique ability to independently and dynamically tune the localization of guided light by engineering the relative effective indices induced by the metasurface nanoantennas.

Figure 4(a) shows the normalized electric field intensity profile $|E|^2$ in the switch for a-Sb_2S_3 at a wavelength 800 nm in

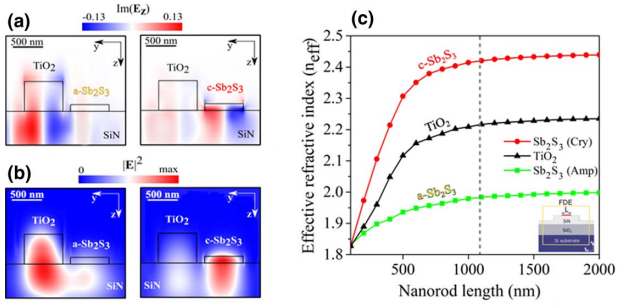

Fig. 3. Characterization of nanoantenna structure. (a) Profile (zy plane) of the normalized near field of the E_z component showing scattering Mie modes in the TiO_2 and Sb_2S_3 nanoantennas for a-Sb_2S_3 (left panel) and c-Sb_2S_3 (right panel) at $\lambda = 800$ nm. (b) Normalized electric field intensity $|E|^2$ distribution (zy plane) in the same nanorods for a-Sb_2S_3 and c-Sb_2S_3. The boundaries of the SiN waveguide and nanoantennas are indicated in solid black lines. (c) Effective refractive index of the TE_{00} mode as a function of TiO_2 nanoantenna length and Sb_2S_3 nanoantenna length for the a-Sb_2S_3 and c-Sb_2S_3 phases. The dashed gray line indicates the length of the nanorods (L) used in our simulation. The inset figure shows the FDE simulation setup.

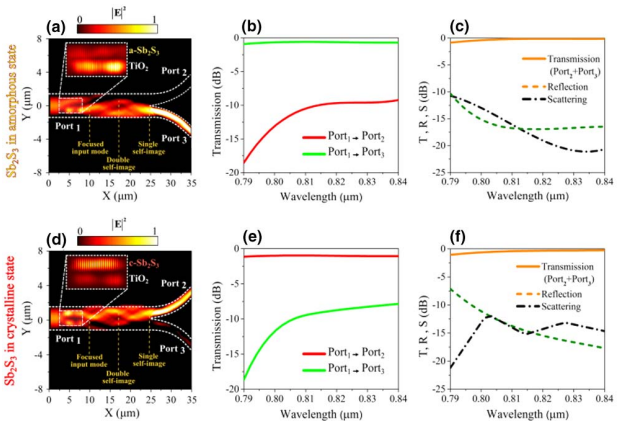

Fig. 4. Simulated device performance for a-Sb_2S_3 (upper panel) and c-Sb_2S_3 (lower panel). (a) and (d) Full-wave simulation showing the optical field intensity $|E|^2$ in the switch for the fundamental TE mode in the *xy* plane at $\lambda = 800$ nm. The boundaries of the SiN waveguide and metasurface structure are indicated by dashed lines and rectangles, respectively. Inset: enlarged view of the field profile in the metasurface. (b) and (e) Transmission spectra at two output ports $Port_2$ and $Port_3$. (c) and (f) Total transmission at output ports ($Port_2 + Port_3$), reflection, and scattering of the device.

the *xy* plane, when the fundamental TE mode is launched from the stem multimode waveguide to the Y branches along the propagation direction (*x* axis). In this case, the field is localized in the TiO_2 nanoantennas as shown in the enlarged view of the inset of Fig. 4(a); the result is consistent with Fig. 3(a), where TiO_2 nanorods show stronger confinement than a-Sb_2S_3 nanorods. Figure 4(b) shows the calculated transmission spectra from $Port_1$ to $Port_2$ and from $Port_1$ to $Port_3$. The average simulated insertion loss in the target port is <0.706 dB. The insertion losses are caused mainly by the reflected optical power resulting from the impedance mismatch with the metasurface nanoantennas and the scattering losses are due to the strong light–antenna interactions at subwavelength intervals. The average value of the cross talk is found to be −11.24 dB throughout the operating bandwidth.

To further characterize the device performance, Fig. 4(c) shows the spectra of total transmission (*T*, $Port_2 + Port_3$), reflection (*R*), and scattering (*S*) over the simulated wavelength region.

Figures 4(d)–4(f) show the functionality of the switch for c-Sb_2S_3. In this case, the field is localized in the c-Sb_2S_3 nanorods because of its stronger light confinement than TiO_2 nanorods [see Fig. 3(b)]. From the calculated transmission spectra in Fig. 4(e), the average value of cross talk is −10.01 dB throughout the operating bandwidth. The average calculated insertion loss is ∼1 dB, which is lower than the efficiency when the switch is in the a-Sb_2S_3. The higher insertion losses are due to increased reflection and scattering losses are because of the higher refractive index of c-Sb_2S_3 compared to a-Sb_2S_3. Figure 4(f) shows the spectra of total transmission (*T*, $Port_2 + Port_3$), reflection (*R*), and scattering (*S*) over the simulated wavelength region. We note that the produced modes at $Port_2$ and $Port_3$ maintain the polarization of the input TE_{00} mode and do not experience any polarization rotation (see Fig. 12 in Appendix G).

4. CONCLUSION

In conclusion, we have proposed a conceptually novel approach for devices that dynamically control guided light using a reconfigurable metasurface. We have demonstrated a broadband compact and low-loss (1 × 2) switch for near-visible wavelengths by integrating a metasurface consisting of two nanorod arrays of TiO_2 and Sb_2S_3 on a silicon nitride waveguide. Our demonstrated device enjoys a record high bandwidth (22.6 THz) compared to other phase-change-material-based switches while having low loss (∼1 dB), low cross talk (−11.24 dB), and ultracompact active length (5.5 μm). The proposed device could be a reliable component in the meshes of future energy-efficient large-scale PICs. Moreover, we believe that integrating active metasurfaces with photonic waveguides, as demonstrated in our example, may provide a step change toward realizing several tunable, efficient, and non-volatile chip-scale devices for applications in neuromorphic computing [5,6], quantum information processing [7,8], optical communication [9,10], microwave photonics [11], and biomedical sensing [12,13].

APPENDIX A: THE DRAWBACKS OF USING LARGE-AREA PCMS FOR DEVICES' ACTUATION MECHANISMS

The use of large-area PCMs creates a considerable barrier to the actuation mechanism because of the following reasons: first, the lack of optimization for additional scaling and integration because of the inaccurate, slow, and diffraction-limited alignment process [85]; second, the difficulty in attaining similar levels of crystallization and amorphization using a thermodynamic mechanism over a large-area PCM [67,86]; third, large-area PCMs prevent achieving the sufficient cooling rate [31,53] that is necessary for the re-amorphization process of PCMs (because PCMs suffer from low thermal conductivity [31,87,88]). These reasons lead to weak and inconsistent switching behavior of large-area PCMs [23,67,86]. In addition, another significant limitation is the filamentation phenomenon associated with electrical switching. Such filamentation causes a nonuniform crystallization throughout large-area PCMs. These limitations eventually lead to devices with weak and inconsistent switching behavior [86,88,89].

A practical solution is reducing the PCMs' volume to the subwavelength scale [31,53,86,88,89]. This solution is adopted from the current well-established phase-change random access memory (PRAM), where the PCM volumes are deeply scaled and embedded in thermally optimized units to achieve the required cooling rate [30,90]. As a result, PRAMs enjoy a high switching cyclability (above 1×10^6) [69] and do not suffer from the filamentation issue [86]. The introduction of PCM-based metasurfaces [27,28,31,86–89,91] represents a viable technological solution for many potential applications. In such a platform (PCM-based metasurfaces), each meta-atom is thermally modulated independently rather than modulating the whole large-area PCM. Hence, the speed and reliability increase

without suffering cooling rate inaccessibility, switching nonuniformity, or crystallization filamentation [27,28,31,86–89,91,92].

APPENDIX B: THE NEED FOR VISIBLE/NEAR-VISIBLE PHOTONIC INTEGRATED DEVICES

The PCM-based integrated devices reported thus far are restricted to the infrared region, where the silicon waveguide exhibits optical transparency and where the PCM (GST and GSST) shows low absorption and high Δn [28]. It is therefore crucially important to realize visible and near-visible integrated photonics that display more compact size, as the footprint of the device relies on the wavelength of its source [93], and to harness the exotic optical phenomena at this spectral region [94], which have been elusive because of the incompatibility with silicon-based PICs due to the high absorption of Si. In addition, visible/near-visible photonic integrated devices are crucial to many applications, particularly in integrated quantum photonics, as quantum light sources, e.g., color centers and quantum dots, emit light in this wavelength range. Also, it is important for biomedical sensing and optogenetics.

APPENDIX C: THE DESIGN OF A STEM MULTIMODE WAVEGUIDE

To study the MMI effect that takes place in our SiN waveguide, it is vital to check the properties of the supported modes in the waveguide. Therefore, in Mode Solutions (Lumerical Ansys Inc), the FDE method was used to calculate the dependence of stem waveguide width (W) on the effective refractive index (n_{eff}) and D of different modes as shown in Figs. 5(a) and 5(b). A wide range of n_{eff} (from 1.72 to 1.878) can be obtained, which corresponds to the propagation constant of supported modes in the waveguide. As it can be seen in Fig. 5(a), the n_{eff} increases rapidly with the increasing W and reaches a maximal constant value [$\max(n_{\mathrm{eff}}) = 1.878$] for the TE_{00} mode. Also, the ∇n_{eff} between the modes decreased with the increasing W. Note that the height (h) of the SiN waveguide is kept constant at 220 nm during the simulation, which is below the maximum value (800 nm) for a crack-free (low pressure chemical vapor deposition, LPCVD) SiN layer [39,95,96]. As we are interested in the TE_{00} mode that is injected into our device, Fig. 5(c) shows the simulated n_{eff} and D curves of the fundamental TE mode in a SiN waveguide with a width 3.5 μm over the simulated wavelengths. In Figs. 5(b) and 5(c) we can see that the waveguide width 3.5 μm features a flat anomalous dispersion for TE_{00} mode over the simulated wavelength. The dependence of waveguide dispersion on the n_{eff} can be given by [97]

$$D = -\frac{\lambda}{c}\frac{\mathrm{d}^2 n_{\mathrm{eff}}}{\mathrm{d}\lambda^2}, \tag{C1}$$

where c is the speed of light in a vacuum.

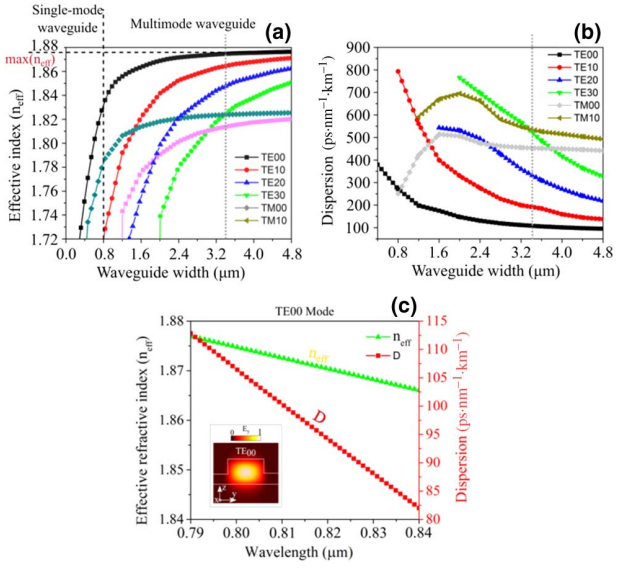

Fig. 5. Multimode waveguide characterization. The dependence of waveguide width on the (a) n_{eff} and (b) dispersion D of different SiN waveguide modes at $\lambda = 800$ nm. The shaded region indicates the waveguide widths that support asymmetric multimode. The dashed black lines show the maximal modal index (n_{eff}) in the waveguide and the waveguide width that support a single mode. The gray dotted line indicates the width considered in the stem SiN waveguide. (c) n_{eff} and D of the fundamental TE_{00} mode as a function of simulated wavelengths. The inset figure shows the E_y distribution of the TE_{00} mode at $\lambda = 800$ nm.

APPENDIX D: THE ROLE OF OPTIMIZING THE HEIGHT AND WIDTH OF TiO_2 IN THE DEVICE PERFORMANCE

To justify the selected dimensions for TiO_2, in Fig. 6, we show the device performance (i.e., cross talk and transmission at the desired output) for c-Sb_2S_3 and a-Sb_2S_3, considering variations in the height and width of TiO_2 nanorods. It is to be noted that the sole reason for increasing the dimensions of TiO_2 nanorods is to optimize the device performance in the amorphous state of Sb_2S_3. As it can be seen in Fig. 6(b), the cross talk decreases notably with the increasing dimensions of TiO_2 nanorods and reaches a global minimum at height 250 nm and width 72 nm. Moreover, the transmission at the desired output in the amorphous state reaches global maximum at the same TiO_2 nanorod dimensions [see Fig. 6(d)].

To further clarify the reason for this behavior, we conducted full-wave simulations to show the propagation of electric field intensity in the device in the crystalline and amorphous states in three different scenarios: (1) the dimensions of the TiO_2 nanorods are exactly the same as those of the Sb_2S_3 nanorods (width = 55 nm, height = 50 nm), (2) the selected TiO_2 nanorods' dimensions (width = 72 nm, height = 250 nm), and (3) the larger TiO_2 nanorods' dimensions (width = 88 nm, height = 300 nm). As it can be seen from the first scenario [Figs. 7(a) and 7(d)], the light remains localized in the Sb_2S_3 nanoantennas (enlarged inset figures) due to its higher refractive index in both phases. This biased localization in the Sb_2S_3 nanorods results in unacceptable performance in the amorphous state because the light is routed to the undesired output. After optimizing the dimensions of the TiO_2 nanorods [Figs. 7(b) and 7(e)], the localization of light changes significantly between the Sb_2S_3/TiO_2 nanorod arrays depending on the phase of Sb_2S_3. Moreover, the produced self-imaged mode takes relatively confined paths in the output ports with

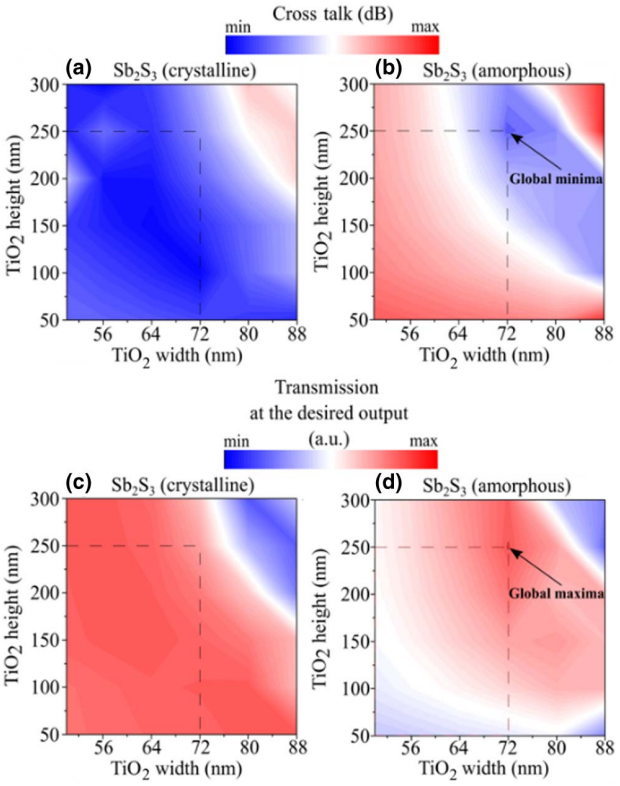

Fig. 6. Parametric sweep of TiO_2 nanorods for the TE_{00} mode at $\lambda = 800$ nm. (a) and (b) Simulated device cross talk considering variations of the height and width of TiO_2 nanorods when Sb_2S_3 is in the crystalline and amorphous state, respectively. (c) and (d) Calculated transmission at the desired output as a function of height and width of TiO_2 nanorods for the crystalline and amorphous state, respectively. The black dashed lines indicate the dimensions used in our metasurface.

high transmittance. Note that the further increase in the dimensions of TiO_2 nanorods [Figs. 7(c) and 7(f)] leads to increased scattering and reflection losses, coupled with altering the position where the self-image is produced.

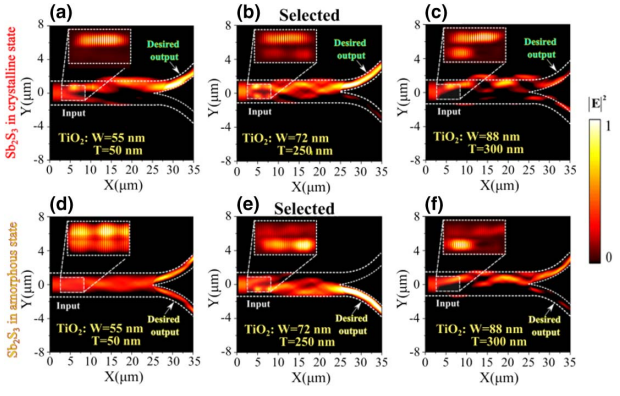

Fig. 7. Full-wave simulation showing the optical field intensity $|E|^2$ in the switch for the fundamental TE mode in the *xy* plane at $\lambda = 800$ nm and for different TiO_2 dimensions for (a)–(c) c-Sb_2S_3 and (d)–(f) a-Sb_2S_3, The boundaries of the SiN waveguide and metasurface structure are indicated by dashed lines and rectangles, respectively. Inset: enlarged view of the field profile in the metasurface.

APPENDIX E: THE SUGGESTED FABRICATION METHOD AND EXPERIMENTAL SETUP OF RECONFIGURABLE METASURFACE-BASED (1 × 2) WAVEGUIDE SWITCH

1. Suggested Fabrication Method

The fabrication of nanorod arrays on top of nanophotonic waveguides was previously described by Yu *et al.* [39] and Wang *et al.* [42]. However, the demonstration of the two nanorod arrays of two different materials patterned on a waveguide has not yet been reported. Therefore, we believe that it is useful to present the fabrication method for this particular design. Figure 8 shows the suggested fabrication process, which can be described as follows. A 3 μm film of silica (SiO_2) is transferred onto a silicon substrate by plasma enhanced chemical vapor deposition (PECVD). A 0.42 μm layer of stoichiometric silicon nitride (SiN) is deposited onto the (SiO_2/Si) wafer using LPCVD. Energy dispersive X-ray spectroscopy (EDX) is used to determine the thickness and composition of the SiN film. The first step of electron beam lithography (EBL; positive resist) is then conducted to pattern the nanorod arrays as well as the alignment marks using JEOL 6300-FX at 250 pA [39]. After the development, a 55 nm film of amorphous Sb_2S_3 is deposited using electron-beam deposition (EBD) and followed by an overnight liftoff using a Microposit Remover 1165 at a temperature of 80°C. The second round of positive resist is conducted to deposit a 250 nm film of TiO_2. To define the SiN waveguide, a second step of EBL (negative resist) is carried out. To pattern the output Y-branch waveguides, an aligned exposure of a beam current (4 nA [39]) is used. After the development, a chromium photomask is deposited onto the wafer via electron-beam evaporation and followed by an overnight liftoff

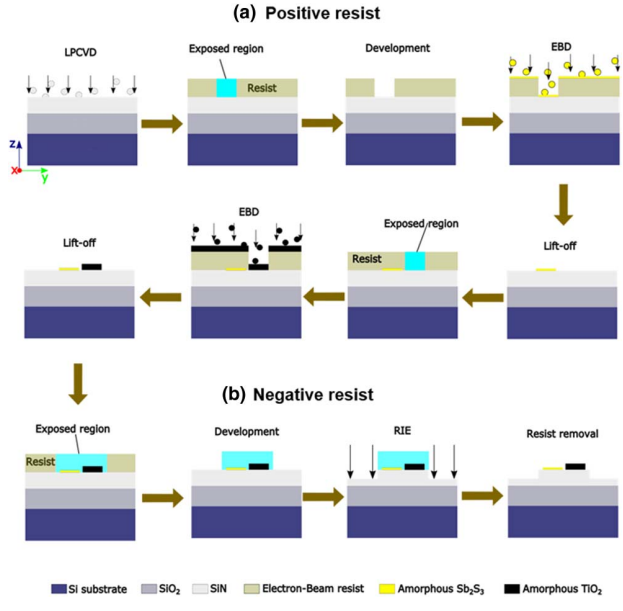

Fig. 8. Suggested fabrication method employing three steps of electron beam lithography: (a) two positive resists followed by LPCVD to transfer the desired patterns of the nanorod arrays onto the developed gaps and (b) a negative resist followed by reactive ion etching (RIE) to define the SiN waveguide.

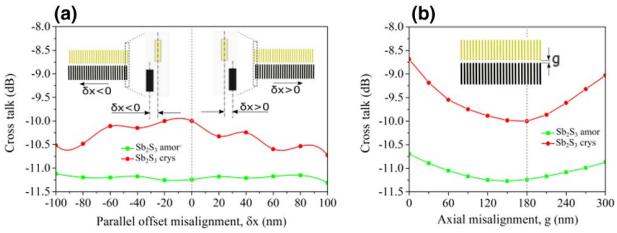

Fig. 9. Device fabrication tolerance. (a) and (b) Simulated device cross talk for the fundamental mode operating at $\lambda = 800$ nm, considering possible parallel misalignment (offset) and axial misalignment (gap width), respectively. The gray dotted lines in the figures indicate the dimensions used in our device.

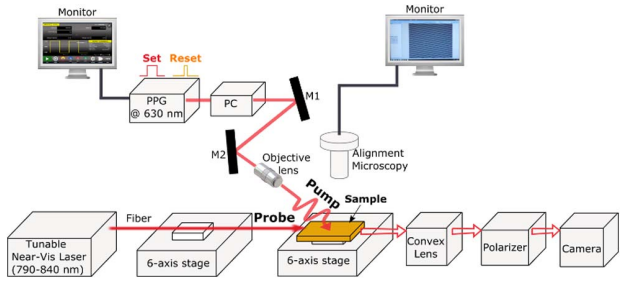

Fig. 10. Schematic illustration of the experimental setup suggested for characterizing the performance of the proposed reconfigurable switch. Here, PPG is a programmable pulse generator, PC is a power controller, and M is a mirror.

using a Microposit Remover 1165 at a temperature of 75°C. To eliminate the residual resist, an oxygen plasma is used at 20°C for 15 s. The SiN waveguides (i.e., stem and Y branches) are etched through the SiN film via plasma reactive ion etching. The residual mask is removed by wet etching [98].

To estimate the device performance against fabrication misalignment between the nanorod arrays in the first and second lithography processes, we simulated the cross-talk response between the output ports considering possible parallel misalignment (offset) [Fig. 9(a)] and axial misalignment (gap) [Fig. 9(b)]. Within the entire calculated dimensions considering both parallel and axial misalignment, the device showed high tolerance to possible nanorod-array misalignments, as the simulated device cross talk showed minor changes in both a-Sb_2S_3 and c-Sb_2S_3. Specifically, for the parallel misalignment, the simulated cross-talk value remained below −10.0 dB, and for the axial misalignment, the cross talk remained below −8.4 dB, even for the worst case, when the nanorod arrays were attached or highly separated from each other. These results confirm the reliability and robustness of our device.

2. Suggested Experimental Setup

Figure 10 illustrates the suggested experimental setup for realizing the reversible optical switching of the Sb_2S_3 and characterizing the switch performance. For optically switching the phase Sb_2S_3, the pump source requires a pulsed diode laser with power of 90 mW working at $\lambda = 630$ nm. The laser pulses are modulated electrically using a programmable pulse generator to produce pulses with varying durations of time. For the crystallization process, long pulses (100 ms) are used, whereas, for the amorphization process, shorter pulses (400 ns) are used [67]. A power controller (PC) composed of a polarizing beam splitter and liquid-crystal retarder is employed to control the power of each pulse [67]. The PC enables increasing the pulses' reproducibility by keeping the diode at a constant current [67]. To obtain the high fluence μm spot size required for the amorphization process, an objective lens is used [67]. In contrast, the spot size is required to slightly be defocused to avoid damage effects in the spot center during the crystallization process [67]. The sample is fixed on a six-axis stage and monitored using alignment microscopy to control the focus of the laser spot precisely [14,39,67]. For the probe source, a tunable near-visible laser injects light to the input port of the switch by butt-coupling [39,42] (alternatively, grating couplers can also be used to couple light from the fiber to the stem SiN waveguide [14]). Convex lenses are used to collect the light that decouples from the output ports of the switch. The polarization controller is employed to ensure matching the fundamental quasi-TE mode of the stem SiN waveguides [14,39,63,85]. Finally, a camera is used for imaging the light spots at the outputs of the switch. Note that if the switch is characterized by an off-chip optical fiber setup using focusing grating couplers at the input and output ports of the switch, then the need for the convex lens is eliminated. And the camera is replaced by a low-noise power meter to measure the power from the output ports [14,19].

APPENDIX F: THE EFFECTIVE INDICES OF A NANOROD-ARRAY-LOADED SiN WAVEGUIDE

The effective refractive indices of each nanorod array in our metasurface were calculated using Rytov's approximation [99] as follows.

The effective indices of Sb_2S_3 nanorod arrays in the amorphous ($n_{as\|}$) and crystalline ($n_{cs\|}$) states can be given by

$$n_{as\|}^2 = \frac{W_{Sb_2S_3}}{\Lambda} n_a^2 + \left(1 - \frac{W_{Sb_2S_3}}{\Lambda}\right) n_{bare}^2, \quad \textbf{(F2)}$$

$$n_{cs\|}^2 = \frac{W_{Sb_2S_3}}{\Lambda} n_c^2 + \left(1 - \frac{W_{Sb_2S_3}}{\Lambda}\right) n_{bare}^2, \quad \textbf{(F3)}$$

where n_a and n_c are the effective indices of a waveguide cross section with a-Sb_2S_3 or c-Sb_2S_3 nanorods, respectively, and n_{bare} is the effective index of a bare SiN waveguide (without nanorods).

The effective index of a TiO_2 nanorod array can be described as

$$n_{t\|}^2 = \frac{W_{TiO_2}}{\Lambda} n_2^2 + \left(1 - \frac{W_{TiO_2}}{\Lambda}\right) n_{bare}^2, \quad \textbf{(F4)}$$

where n_2 is the effective index of waveguide cross section with a TiO_2 nanorod.

Figures 11(a)–11(c) schematically illustrate x-periodic nanoantenna arrays patterned on a SiN waveguide. We started by calculating the effective indices of the bare SiN waveguide as well as the nanorod-loaded waveguide using the FDE solver (Lumerical Inc.) as shown in Fig. 11(d). Following that, we employed Rytov's formulas to calculate the effective indices

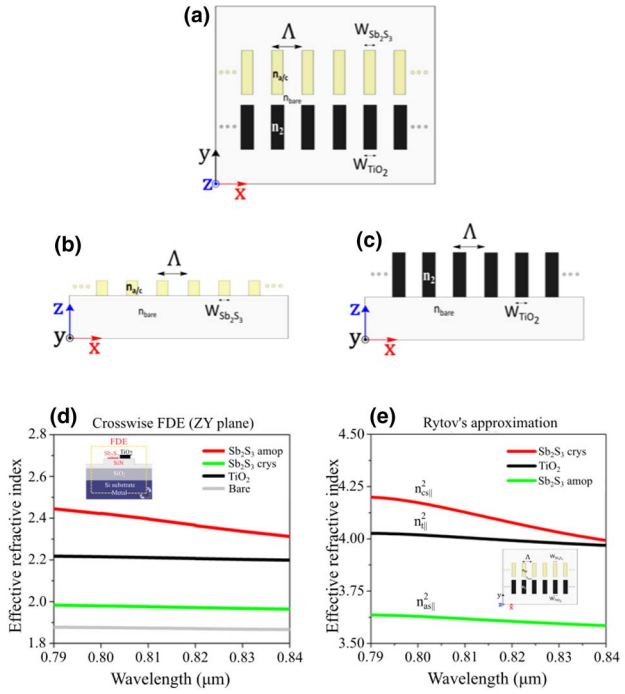

Fig. 11. Sketches showing x-periodic Sb_2S_3 and TiO_2 nanoantennas patterned on a SiN waveguide in (a) xy plane and (b), (c) zy plane, where $n_{a/c}$ are the effective indices of a-Sb_2S_3 and c-Sb_2S_3 nanorods, n_2 is the effective index of the TiO_2 nanorods, and n_{bare} is the effective index of bare SiN waveguide. (d) Effective refractive indices for the waveguide cross section calculated using FDE. The inset shows the FDE simulation setup. (e) Effective indices for nanorod arrays calculated by Rytov's approximation.

of the periodic nanorod arrays. As shown in Fig. 11(e), the magnitude of the effective index of a TiO_2 nanorod array is larger than that of a-Sb_2S_3 after optimizing their dimensions as discussed in the previous section.

APPENDIX G: MODAL PROFILES AT THE DEVICE INPUT AND OUTPUT PORTS

It is important to note that the produced modes at the output ports of the device maintain the polarization of the input TE_{00} mode in both Sb_2S_3 phases. Figure 12(a–c) shows the electric field component E_y for TE_{00} mode at the input and output ports of the device. The arrows illustrate the corresponding vector diagrams of the electric fields of the modes at the input and output ports.

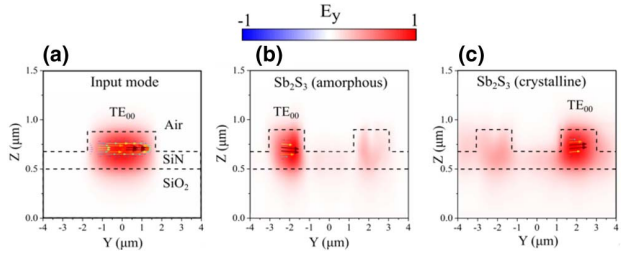

Fig. 12. Modes in the input and output ports of SiN waveguides. Simulated E_y component at $\lambda = 800$ nm for the TE_{00} mode in the (a) input stem SiN waveguide before interacting with the metasurface, (b) output $Port_3$ for a-Sb_2S_3 and (c) output $Port_2$ for c-Sb_2S_3. The arrows indicate the vector diagrams of the electric field component of the modes. The dashed black lines show the boundaries of the SiN waveguides.

Funding. CAS-TWAS Presidents Fellowship Program; National Natural Science Foundation of China (62134009, 62121005); Innovation Grant of Changchun Institute of Optics, Fine Mechanics and Physics (CIOMP); Jilin Provincial Science and Technology Development Project (YDZJ202102CXJD002); Development Program of the Science and Technology of Jilin Province (20200802001GH); Scientific Research Project of the Chinese Academy of Sciences (QYZDB-SSW-SYS038).

Acknowledgment. A. A. acknowledges the CAS-TWAS Presidents Fellowship Program. M. E. initiated the project and conceived the approach. C. G., W. L., M. E., and J. C. supervised the project. A. A. designed the metasurface and performed simulations. A. A., M. E., W. L., J. C., and G. V. analyzed the data. C. S. contributed to the discussions. A. A. wrote the paper with input from all the authors. All authors discussed the research.

Disclosures. The authors declare no conflicts of interest.

Data Availability. The data that support the findings of this study are available from the corresponding author upon reasonable request.

REFERENCES

1. B. J. Shastri, A. N. Tait, T. Ferreira de Lima, W. H. P. Pernice, H. Bhaskaran, C. D. Wright, and P. R. Prucnal, "Photonics for artificial intelligence and neuromorphic computing," Nat. Photonics **15**, 102–114 (2021).
2. Z. Chen and M. Segev, "Highlighting photonics: looking into the next decade," eLight **1**, 2 (2021).
3. G. Wetzstein, A. Ozcan, S. Gigan, S. Fan, D. Englund, M. Soljačić, C. Denz, D. A. B. Miller, and D. Psaltis, "Inference in artificial intelligence with deep optics and photonics," Nature **588**, 39–47 (2020).
4. W. Bogaerts, D. Pérez, J. Capmany, D. A. B. Miller, J. Poon, D. Englund, F. Morichetti, and A. Melloni, "Programmable photonic circuits," Nature **586**, 207–216 (2020).
5. J. Feldmann, N. Youngblood, C. D. Wright, H. Bhaskaran, and W. H. P. Pernice, "All-optical spiking neurosynaptic networks with self-learning capabilities," Nature **569**, 208–214 (2019).
6. J. Torrejon, M. Riou, F. A. Araujo, S. Tsunegi, G. Khalsa, D. Querlioz, P. Bortolotti, V. Cros, K. Yakushiji, A. Fukushima, H. Kubota, S. Yuasa, M. D. Stiles, and J. Grollier, "Neuromorphic computing with nanoscale spintronic oscillators," Nature **547**, 428–431 (2017).
7. J. Wang, F. Sciarrino, A. Laing, and M. G. Thompson, "Integrated photonic quantum technologies," Nat. Photonics **14**, 273–284 (2020).
8. A. Blais, S. M. Girvin, and W. D. Oliver, "Quantum information processing and quantum optics with circuit quantum electrodynamics," Nat. Phys. **16**, 247–256 (2020).
9. S. Leedumrongwatthanakun, L. Innocenti, H. Defienne, T. Juffmann, A. Ferraro, M. Paternostro, and S. Gigan, "Programmable linear quantum networks with a multimode fibre," Nat. Photonics **14**, 139–142 (2020).
10. Q. Ma, L. Chen, H. B. Jing, Q. R. Hong, H. Y. Cui, Y. Liu, L. Li, and T. J. Cui, "Controllable and programmable nonreciprocity based on detachable digital coding metasurface," Adv. Opt. Mater. **7**, 1901285 (2019).

11. D. Marpaung, J. Yao, and J. Capmany, "Integrated microwave photonics," Nat. Photonics **13**, 80–90 (2019).
12. Y. Wang, W. Li, M. Li, S. Zhao, F. De Ferrari, M. Liscidini, and F. G. Omenetto, "Biomaterial-based 'structured opals' with programmable combination of diffractive optical elements and photonic bandgap effects," Adv. Mater. **31**, 1805312 (2019).
13. Z. Li, J. Zou, H. Zhu, B. T. T. Nguyen, Y. Shi, P. Y. Liu, R. C. Bailey, J. Zhou, H. Wang, Z. Yang, Y. Jin, P. H. Yap, H. Cai, Y. Hao, and A. Q. Liu, "Biotoxoid photonic sensors with temperature insensitivity using a cascade of ring resonator and Mach–Zehnder interferometer," ACS Sens. **5**, 2448–2456 (2020).
14. P. Xu, J. Zheng, J. K. Doylend, and A. Majumdar, "Low-loss and broadband nonvolatile phase-change directional coupler switches," ACS Photon. **6**, 553–557 (2019).
15. M. Rudé, J. Pello, R. E. Simpson, J. Osmond, G. Roelkens, J. J. G. M. van der Tol, and V. Pruneri, "Optical switching at 1.55 μm in silicon racetrack resonators using phase change materials," Appl. Phys. Lett. **103**, 141119 (2013).
16. M. Stegmaier, C. Ríos, H. Bhaskaran, C. D. Wright, and W. H. P. Pernice, "Nonvolatile all-optical 1 × 2 switch for chipscale photonic networks," Adv. Opt. Mater. **5**, 1600346 (2017).
17. J. Zheng, A. Khanolkar, P. Xu, S. Colburn, S. Deshmukh, J. Myers, J. Frantz, E. Pop, J. Hendrickson, J. Doylend, N. Boechler, and A. Majumdar, "GST-on-silicon hybrid nanophotonic integrated circuits: a non-volatile quasi-continuously reprogrammable platform," Opt. Mater. Express **8**, 1551–1561 (2018).
18. Y. Zhang, J. B. Chou, J. Li, H. Li, Q. Du, A. Yadav, S. Zhou, M. Y. Shalaginov, Z. Fang, H. Zhong, C. Roberts, P. Robinson, B. Bohlin, C. Ríos, H. Lin, M. Kang, T. Gu, J. Warner, V. Liberman, K. Richardson, and J. Hu, "Broadband transparent optical phase change materials for high-performance nonvolatile photonics," Nat. Commun. **10**, 4279 (2019).
19. C. Wu, H. Yu, H. Li, X. Zhang, I. Takeuchi, and M. Li, "Low-loss integrated photonic switch using subwavelength patterned phase change material," ACS Photon. **6**, 87–92 (2019).
20. C. Zhang, M. Zhang, Y. Xie, Y. Shi, R. Kumar, R. R. Panepucci, and D. Dai, "Wavelength-selective 2×2 optical switch based on a $Ge_2Sb_2Te_5$-assisted microring," Photon. Res. **8**, 1171–1176 (2020).
21. T. J. Seok, N. Quack, S. Han, R. S. Muller, and M. C. Wu, "Large-scale broadband digital silicon photonic switches with vertical adiabatic couplers," Optica **3**, 64–70 (2016).
22. T. J. Seok, J. Luo, Z. Huang, K. Kwon, J. Henriksson, J. Jacobs, L. Ochikubo, R. S. Muller, and M. C. Wu, "Silicon photonic wavelength cross-connect with integrated MEMS switching," APL Photon. **4**, 100803 (2019).
23. J. Zheng, S. Zhu, P. Xu, S. Dunham, and A. Majumdar, "Modeling electrical switching of nonvolatile phase-change integrated nanophotonic structures with graphene heaters," ACS Appl. Mater. Interfaces **12**, 21827–21836 (2020).
24. M. Ono, M. Hata, M. Tsunekawa, K. Nozaki, H. Sumikura, H. Chiba, and M. Notomi, "Ultrafast and energy-efficient all-optical switching with graphene-loaded deep-subwavelength plasmonic waveguides," Nat. Photonics **14**, 37–43 (2020).
25. M. Thomaschewski, V. A. Zenin, C. Wolff, and S. I. Bozhevolnyi, "Plasmonic monolithic lithium niobate directional coupler switches," Nat. Commun. **11**, 748 (2020).
26. D. Pérez, I. Gasulla, P. Das Mahapatra, and J. Capmany, "Principles, fundamentals, and applications of programmable integrated photonics," Adv. Opt. Photon. **12**, 709–786 (2020).
27. M. Wuttig, H. Bhaskaran, and T. Taubner, "Phase-change materials for non-volatile photonic applications," Nat. Photonics **11**, 465–476 (2017).
28. S. Abdollahramezani, O. Hemmatyar, H. Taghinejad, A. Krasnok, Y. Kiarashinejad, M. Zandehshahvar, A. Alù, and A. Adibi, "Tunable nanophotonics enabled by chalcogenide phase-change materials," Nanophotonics **9**, 1189–1241 (2020).
29. N. Farmakidis, N. Youngblood, X. Li, J. Tan, J. L. Swett, Z. Cheng, C. D. Wright, W. H. P. Pernice, and H. Bhaskaran, "Plasmonic nanogap enhanced phase-change devices with dual electrical-optical functionality," Sci. Adv. **5**, eaaw2687 (2019).
30. D. Loke, T. H. Lee, W. J. Wang, L. P. Shi, R. Zhao, Y. C. Yeo, T. C. Chong, and S. R. Elliott, "Breaking the speed limits of phase-change memory," Science **336**, 1566 (2012).
31. C. R. de Galarreta, A. M. Alexeev, Y.-Y. Au, M. Lopez-Garcia, M. Klemm, M. Cryan, J. Bertolotti, and C. D. Wright, "Nonvolatile reconfigurable phase-change metadevices for beam steering in the near infrared," Adv. Funct. Mater. **28**, 1704993 (2018).
32. C. Rios, P. Hosseini, C. D. Wright, H. Bhaskaran, and W. H. P. Pernice, "On-chip photonic memory elements employing phase-change materials," Adv. Mater. **26**, 1372–1377 (2014).
33. Z. Cheng, C. Ríos, N. Youngblood, C. D. Wright, W. H. P. Pernice, and H. Bhaskaran, "Device-level photonic memories and logic applications using phase-change materials," Adv. Mater. **30**, 1802435 (2018).
34. M. A. Kats, D. Sharma, J. Lin, P. Genevet, R. Blanchard, Z. Yang, M. M. Qazilbash, D. N. Basov, S. Ramanathan, and F. Capasso, "Ultra-thin perfect absorber employing a tunable phase change material," Appl. Phys. Lett. **101**, 221101 (2012).
35. H. Liang, R. Soref, J. Mu, A. Majumdar, X. Li, and W.-P. Huang, "Simulations of silicon-on-insulator channel-waveguide electrooptical 2 × 2 switches and 1 × 1 modulators using a $Ge_2Sb_2Te_5$ self-holding layer," J. Lightwave Technol. **33**, 1805–1813 (2015).
36. J. Feldmann, M. Stegmaier, N. Gruhler, C. Ríos, H. Bhaskaran, C. D. Wright, and W. H. P. Pernice, "Calculating with light using a chip-scale all-optical abacus," Nat. Commun. **8**, 1256 (2017).
37. M. Xu, X. Mai, J. Lin, W. Zhang, Y. Li, Y. He, H. Tong, X. Hou, P. Zhou, and X. Miao, "Recent advances on neuromorphic devices based on chalcogenide phase-change materials," Adv. Funct. Mater. **30**, 2003419 (2020).
38. A. H. Dorrah, N. A. Rubin, A. Zaidi, M. Tamagnone, and F. Capasso, "Metasurface optics for on-demand polarization transformations along the optical path," Nat. Photonics **15**, 287–296 (2021).
39. Z. Li, M.-H. Kim, C. Wang, Z. Han, S. Shrestha, A. C. Overvig, M. Lu, A. Stein, A. M. Agarwal, M. Lončar, and N. Yu, "Controlling propagation and coupling of waveguide modes using phase-gradient metasurfaces," Nat. Nanotechnol. **12**, 675–683 (2017).
40. B. Wang, S. Blaize, and R. Salas-Montiel, "Nanoscale plasmonic TM-pass polarizer integrated on silicon photonics," Nanoscale **11**, 20685–20692 (2019).
41. A. Alquliah, M. Elkabbash, J. Zhang, J. Cheng, and C. Guo, "Ultrabroadband, compact, polarization independent and efficient metasurface-based power splitter on lithium niobate waveguides," Opt. Express **29**, 8160–8170 (2021).
42. C. Wang, Z. Li, M.-H. Kim, X. Xiong, X.-F. Ren, G.-C. Guo, N. Yu, and M. Lončar, "Metasurface-assisted phase-matching-free second harmonic generation in lithium niobate waveguides," Nat. Commun. **8**, 2098 (2017).
43. V. Ginis, M. Piccardo, M. Tamagnone, J. Lu, M. Qiu, S. Kheifets, and F. Capasso, "Remote structuring of near-field landscapes," Science **369**, 436–440 (2020).
44. X. Guo, Y. Ding, X. Chen, Y. Duan, and X. Ni, "Molding free-space light with guided wave–driven metasurfaces," Sci. Adv. **6**, eabb4142 (2020).
45. R. Guo, M. Decker, F. Setzpfandt, X. Gai, D.-Y. Choi, R. Kiselev, A. Chipouline, I. Staude, T. Pertsch, D. N. Neshev, and Y. S. Kivshar, "High–bit rate ultra-compact light routing with mode-selective on-chip nanoantennas," Sci. Adv. **3**, e1700007 (2017).
46. S. Sun, Q. He, S. Xiao, Q. Xu, X. Li, and L. Zhou, "Gradient-index meta-surfaces as a bridge linking propagating waves and surface waves," Nat. Mater. **11**, 426–431 (2012).
47. A. M. Shaltout, V. M. Shalaev, and M. L. Brongersma, "Spatiotemporal light control with active metasurfaces," Science **364**, eaat3100 (2019).
48. O. Tsilipakos, A. C. Tasolamprou, A. Pitilakis, F. Liu, X. Wang, M. S. Mirmoosa, D. C. Tzarouchis, S. Abadal, H. Taghvaee, C. Liaskos, A. Tsioliaridou, J. Georgiou, A. Cabellos-Aparicio, E. Alarcón, S. Ioannidis, A. Pitsillides, I. F. Akyildiz, N. V. Kantartzis, E. N. Economou, C. M. Soukoulis, M. Kafesaki, and S. Tretyakov, "Toward intelligent metasurfaces: the progress from globally tunable metasurfaces to software-defined metasurfaces with an embedded network of controllers," Adv. Opt. Mater. **8**, 2000783 (2020).
49. F. Ding, Y. Yang, and S. I. Bozhevolnyi, "Dynamic metasurfaces using phase-change chalcogenides," Adv. Opt. Mater. **7**, 1801709 (2019).

50. Q. Wang, E. T. F. Rogers, B. Gholipour, C.-M. Wang, G. Yuan, J. Teng, and N. I. Zheludev, "Optically reconfigurable metasurfaces and photonic devices based on phase change materials," Nat. Photonics **10**, 60–65 (2016).
51. S. G.-C. Carrillo, L. Trimby, Y.-Y. Au, V. K. Nagareddy, G. Rodriguez-Hernandez, P. Hosseini, C. Ríos, H. Bhaskaran, and C. D. Wright, "A nonvolatile phase-change metamaterial color display," Adv. Opt. Mater. **7**, 1801782 (2019).
52. Z. Zhu, P. G. Evans, R. F. Haglund, and J. G. Valentine, "Dynamically reconfigurable metadevice employing nanostructured phase-change materials," Nano Lett. **17**, 4881–4885 (2017).
53. C. Ruiz de Galarreta, I. Sinev, A. M. Alexeev, P. Trofimov, K. Ladutenko, S. G.-C. Carrillo, E. Gemo, A. Baldycheva, J. Bertolotti, and C. D. Wright, "Reconfigurable multilevel control of hybrid all-dielectric phase-change metasurfaces," Optica **7**, 476–484 (2020).
54. T. J. Cui, M. Q. Qi, X. Wan, J. Zhao, and Q. Cheng, "Coding metamaterials, digital metamaterials and programmable metamaterials," Light Sci. Appl. **3**, e218 (2014).
55. L. Zhang, M. Z. Chen, W. Tang, J. Y. Dai, L. Miao, X. Y. Zhou, S. Jin, Q. Cheng, and T. J. Cui, "A wireless communication scheme based on space- and frequency-division multiplexing using digital metasurfaces," Nat. Electron. **4**, 218–227 (2021).
56. L. Li, Y. Shuang, Q. Ma, H. Li, H. Zhao, M. Wei, C. Liu, C. Hao, C.-W. Qiu, and T. J. Cui, "Intelligent metasurface imager and recognizer," Light Sci. Appl. **8**, 97 (2019).
57. R.-B. Hwang, "Binary meta-hologram for a reconfigurable holographic metamaterial antenna," Sci. Rep. **10**, 8586 (2020).
58. C. Liu, W. M. Yu, Q. Ma, L. Li, and T. J. Cui, "Intelligent coding metasurface holograms by physics-assisted unsupervised generative adversarial network," Photon. Res. **9**, B159–B167 (2021).
59. J. Xiong and S.-T. Wu, "Planar liquid crystal polarization optics for augmented reality and virtual reality: from fundamentals to applications," eLight **1**, 3 (2021).
60. X. G. Zhang, W. X. Jiang, H. L. Jiang, Q. Wang, H. W. Tian, L. Bai, Z. J. Luo, S. Sun, Y. Luo, C.-W. Qiu, and T. J. Cui, "An optically driven digital metasurface for programming electromagnetic functions," Nat. Electron. **3**, 165–171 (2020).
61. Q. Zhang, Y. Zhang, J. Li, R. Soref, T. Gu, and J. Hu, "Broadband nonvolatile photonic switching based on optical phase change materials: beyond the classical figure-of-merit," Opt. Lett. **43**, 94–97 (2018).
62. H. Hu, H. Zhang, L. Zhou, J. Xu, L. Lu, J. Chen, and B. M. A. Rahman, "Contra-directional switching enabled by Si-GST grating," Opt. Express **28**, 1574–1584 (2020).
63. Z. Fang, J. Zheng, A. Saxena, J. Whitehead, Y. Chen, and A. Majumdar, "Non-volatile reconfigurable integrated photonics enabled by broadband low-loss phase change material," Adv. Opt. Mater. **9**, 2002049 (2021).
64. X. Li, N. Youngblood, Z. Cheng, S. G.-C. Carrillo, E. Gemo, W. H. P. Pernice, C. D. Wright, and H. Bhaskaran, "Experimental investigation of silicon and silicon nitride platforms for phase-change photonic in-memory computing," Optica **7**, 218–225 (2020).
65. W. Dong, H. Liu, J. K. Behera, L. Lu, R. J. H. Ng, K. V. Sreekanth, X. Zhou, J. K. W. Yang, and R. E. Simpson, "Wide bandgap phase change material tuned visible photonics," Adv. Funct. Mater. **29**, 1806181 (2019).
66. K. V. Sreekanth, Q. Ouyang, S. Sreejith, S. Zeng, W. Lishu, E. Ilker, W. Dong, M. ElKabbash, Y. Ting, C. T. Lim, M. Hinczewski, G. Strangi, K.-T. Yong, R. E. Simpson, and R. Singh, "Phase-change-material-based low-loss visible-frequency hyperbolic metamaterials for ultrasensitive label-free biosensing," Adv. Opt. Mater. **7**, 1900081 (2019).
67. M. Delaney, I. Zeimpekis, D. Lawson, D. W. Hewak, and O. L. Muskens, "A new family of ultralow loss reversible phase-change materials for photonic integrated circuits: Sb_2S_3 and Sb_2Se_3," Adv. Funct. Mater. **30**, 2002447 (2020).
68. W. Zhu, R. Yang, G. Geng, Y. Fan, X. Guo, P. Li, Q. Fu, F. Zhang, C. Gu, and J. Li, "Titanium dioxide metasurface manipulating high-efficiency and broadband photonic spin Hall effect in visible regime," Nanophotonics **9**, 4327–4335 (2020).
69. M. Wuttig and N. Yamada, "Phase-change materials for rewriteable data storage," Nat. Mater. **6**, 824–832 (2007).
70. K. R. Safronov, D. N. Gulkin, I. M. Antropov, K. A. Abrashitova, V. O. Bessonov, and A. A. Fedyanin, "Multimode interference of Bloch surface electromagnetic waves," ACS Nano **14**, 10428–10437 (2020).
71. P. Sethi, A. Haldar, and S. K. Selvaraja, "Ultra-compact low-loss broadband waveguide taper in silicon-on-insulator," Opt. Express **25**, 10196–10203 (2017).
72. Y. Fu, T. Ye, W. Tang, and T. Chu, "Efficient adiabatic silicon-on-insulator waveguide taper," Photon. Res. **2**, A41–A44 (2014).
73. J. Zhang, J. Yang, H. Xin, J. Huang, D. Chen, and Z. Zhaojian, "Ultrashort and efficient adiabatic waveguide taper based on thin flat focusing lenses," Opt. Express **25**, 19894–19903 (2017).
74. C. Sun, Y. Yu, and X. Zhang, "Ultra-compact waveguide crossing for a mode-division multiplexing optical network," Opt. Lett. **42**, 4913–4916 (2017).
75. Y. Zhang, Y. He, H. Wang, L. Sun, and Y. Su, "Ultra-broadband mode size converter using on-chip metamaterial-based Luneburg lens," ACS Photon. **8**, 202–208 (2021).
76. J. M. Luque-González, R. Halir, J. G. Wangüemert-Pérez, J. de-Oliva-Rubio, J. H. Schmid, P. Cheben, Í. Molina-Fernández, and A. Ortega-Moñux, "An ultracompact GRIN-lens-based spot size converter using subwavelength grating metamaterials," Laser Photon. Rev. **13**, 1900172 (2019).
77. C. Yao, S. C. Singh, M. ElKabbash, J. Zhang, H. Lu, and C. Guo, "Quasi-rhombus metasurfaces as multimode interference couplers for controlling the propagation of modes in dielectric-loaded waveguides," Opt. Lett. **44**, 1654–1657 (2019).
78. E. D. Palik, *Handbook of Optical Constants of Solids* (Academic, 2012).
79. M. Delaney, I. Zeimpekis, D. Lawson, D. Hewak, and O. Muskens, "A new family of ultra-low loss reversible phase change materials for photonic integrated circuits: Sb_2S_3 and Sb_2Se_3," Adv. Funct. Mater. **30**, 2002447 (2020).
80. M. M. R. Elsawy, S. Lanteri, R. Duvigneau, J. A. Fan, and P. Genevet, "Numerical optimization methods for metasurfaces," Laser Photon. Rev. **14**, 1900445 (2020).
81. K. Koshelev and Y. Kivshar, "Dielectric resonant metaphotonics," ACS Photon. **8**, 102–112 (2021).
82. I. Staude, T. Pertsch, and Y. S. Kivshar, "All-dielectric resonant meta-optics lightens up," ACS Photon. **6**, 802–814 (2019).
83. R. Halir, P. J. Bock, P. Cheben, A. Ortega-Moñux, C. Alonso-Ramos, J. H. Schmid, J. Lapointe, D.-X. Xu, J. G. Wangüemert-Pérez, Í. Molina-Fernández, and S. Janz, "Waveguide sub-wavelength structures: a review of principles and applications," Laser Photon. Rev. **9**, 25–49 (2015).
84. P. Cheben, R. Halir, J. H. Schmid, H. A. Atwater, and D. R. Smith, "Subwavelength integrated photonics," Nature **560**, 565–572 (2018).
85. J. Zheng, Z. Fang, C. Wu, S. Zhu, P. Xu, J. K. Doylend, S. Deshmukh, E. Pop, S. Dunham, M. Li, and A. Majumdar, "Nonvolatile electrically reconfigurable integrated photonic switch enabled by a silicon PIN diode heater," Adv. Mater. **32**, 2001218 (2020).
86. Y. Zhang, C. Ríos, M. Y. Shalaginov, M. Li, A. Majumdar, T. Gu, and J. Hu, "Myths and truths about optical phase change materials: a perspective," Appl. Phys. Lett. **118**, 210501 (2021).
87. K. Shportko, S. Kremers, M. Woda, D. Lencer, J. Robertson, and M. Wuttig, "Resonant bonding in crystalline phase-change materials," Nat. Mater. **7**, 653–658 (2008).
88. Y. Wang, P. Landreman, D. Schoen, K. Okabe, A. Marshall, U. Celano, H. S. P. Wong, J. Park, and M. L. Brongersma, "Electrical tuning of phase-change antennas and metasurfaces," Nat. Nanotechnol. **16**, 667–672 (2021).
89. Y. Zhang, C. Fowler, J. Liang, B. Azhar, M. Y. Shalaginov, S. Deckoff-Jones, S. An, J. B. Chou, C. M. Roberts, V. Liberman, M. Kang, C. Ríos, K. A. Richardson, C. Rivero-Baleine, T. Gu, H. Zhang, and J. Hu, "Electrically reconfigurable non-volatile metasurface using low-loss optical phase-change material," Nat. Nanotechnol. **16**, 661–666 (2021).
90. T. Akiyama, M. Uno, H. Kitaura, K. Narumi, R. Kojima, K. Nishiuchi, and N. Yamada, "Rewritable dual-layer phase-change optical disk utilizing a blue-violet laser," Jpn. J. Appl. Phys. **40**, 1598–1603 (2001).

91. W. Zhang, R. Mazzarello, M. Wuttig, and E. Ma, "Designing crystallization in phase-change materials for universal memory and neuro-inspired computing," Nat. Rev. Mater. **4**, 150–168 (2019).
92. C. R. De Galarreta Fanjul, "Reconfigurable phase-change optical metasurfaces: novel design concepts to practicable devices," Ph.D. thesis (University of Exeter, 2020).
93. P. Trofimov, A. P. Pushkarev, I. S. Sinev, V. V. Fedorov, S. Bruyère, A. Bolshakov, I. S. Mukhin, and S. V. Makarov, "Perovskite–gallium phosphide platform for reconfigurable visible-light nanophotonic chip," ACS Nano **14**, 8126–8134 (2020).
94. B. Desiatov, A. Shams-Ansari, M. Zhang, C. Wang, and M. Lončar, "Ultra-low-loss integrated visible photonics using thin-film lithium niobate," Optica **6**, 380–384 (2019).
95. H. M. Mbonde, H. C. Frankis, and J. D. B. Bradley, "Enhanced nonlinearity and engineered anomalous dispersion in TeO_2-coated Si_3N_4 waveguides," IEEE Photon. J. **12**, 2200210 (2020).
96. H. El Dirani, L. Youssef, C. Petit-Etienne, S. Kerdiles, P. Grosse, C. Monat, E. Pargon, and C. Sciancalepore, "Ultralow-loss tightly confining Si_3N_4 waveguides and high-Q microresonators," Opt. Express **27**, 30726–30740 (2019).
97. R. R. Grote and L. C. Bassett, "Single-mode optical waveguides on native high-refractive-index substrates," APL Photon. **1**, 071302 (2016).
98. K. Bi, Q. Wang, J. Xu, L. Chen, C. Lan, and M. Lei, "All-dielectric metamaterial fabrication techniques," Adv. Opt. Mater. **9**, 2001474 (2021).
99. S. Rytov, "Electromagnetic properties of a finely stratified medium," J. Exp. Theor. Phys. **2**, 466–475 (1956).